The supplementary information for the paper:

Micro-pixelated halide perovskite photodiodes fabricated with ultraviolet laser scribing

A.P. Morozov[1,2], P.A. Gostishchev[1,2], A. Zharkova[1], A.A. Vasilev[3], A.E. Aleksandrov[4], L.O. Luchnikov[1], A.R. Tameev[4], D.A. Kiselev[5], T.S. Ilina[5], A.R. Ishteev[1], S.I. Didenko[3] and D.S. Saranin[1*]

[1]LASE – Laboratory of Advanced Solar Energy, NUST MISiS, 119049 Moscow, Russia

[2]Research and Practical Clinical Center for Diagnostics and Telemedicine Technologies of the Moscow Health Care Department, Petrovka str., 24, Moscow, Russia 127051

[3]Department of semiconductor electronics and device physics, NUST MISiS, 119049 Moscow, Russia

[4]Laboratory "Electronic and photon processes in polymer nanomaterials", Russian Academy of Sciences A.N. Frumkin Institute of Physical chemistry and Electrochemistry, 119071, Moscow, Russia

[5]Laboratory of Physics of Oxide Ferroelectrics, Department of Materials Science of Semiconductors and Dielectrics, National University of Science and Technology MISIS, Moscow 119049, Russia

Corresponding author: Dr. Danila S. Saranin saranin.ds@misis.ru

Experimental section:

Materials

All organic solvents—dimethylformamide (DMF), N-Methylpyrrolidone (NMP), isopropyl alcohol (IPA), chlorobenzene (CB) were purchased in anhydrous, ultra-pure grade from Sigma Aldrich, and used as received. Ethylacetate (EAC, 99+% purity) was purchased from Reaktivtorg-Himprocess hps, 2-Methoxyethanol was purchased from Acros Organics (99.5+%, for analysis), HNO_3 (70%). Photodiodes were fabricated on In_2O_3: SnO_2 (ITO) coated glass (R_{sheet}<7 Ohm/sq) from Zhuhai Kaivo company (China). $NiCl_2 \cdot 6H_2O$ (from ReaktivTorg 99+% purity) used for HTM fabrication. Lead Iodide (99.9%), Cesium iodide (99.99%), Cesium chloride (99.99%) trace metals basis from LLC Lanhit, Russia and formamidinium iodide (FAI, 99.99% purity from GreatcellSolar), were used for perovskite ink. [6,6]-Phenyl-C61-butyric acid methyl ester (99% purity) was purchased from MST NANO (Russia). Bathocuproine (BCP, >99.8% sublimed grade) was purchased from Osilla Inc. (UK) and used for the fabrication of hole blocking layer.

Inks preparation

For the preparation of composition $Cs_{0.2}FA_{0.8}PbI_{2.93}Cl_{0.07}$ perovskite ink, we used CsCl, CsI, FAI, PbI_2 powders in a 0.07:0.13:0.8:1molar ratio. The resulting mixture was dissolved in a DMF:NMP (volume ratio 640:360) with a concentration of 1.35 M and stirred at a temperature of 50 °C for 1 h. PCBM was dissolved in CBat a concentration of 27 mg/ml and stirred for 1 h at a temperature of 50 °C. BCP was dissolved in IPA at a concentration of 0.5 mg/ml and stirred for 8 h at a temperature of 50 °C. Before use, all solutions were filtered through 0.45 μm PTFE filters.

Device fabrication

Perovskite photodiodes were fabricated with inverted planar architecture ITO/c-NiO /perovskite ($Cs0.2FA0.8PbI_{2.93}Cl_{0.07}$)/PCBM/BCP/Cu. Firstly, the patterned ITO substrates were cleaned with detergent, de-ionized water, acetone, and IPA in the ultrasonic bath. Then, substrates were activated under UV-ozone irradiation for 30 min. $NiCl_2 \cdot 6H_2O$ precursor for NiO HTM film was spin-coated at 4000 RPMs (30 s), dried at 120 °C (10 min), and annealed at 300 °C (1 h) in the ambient atmosphere. Perovskite absorber film was crystallized on the top of HTM with solvent

engineering method. Perovskite precursor was spin-coated at 3000 RPMs (5 s), and 5000 RPMs (30 s), 200 μL of EAC were poured on the substrate on the 21st second after the start of the rotation process. Then, substrates were annealed at 85 °C (1 min) and 105 °C (30 min) for conversation into the black perovskite phase. The PCBM ETL was spin-coated at RPMs (30 s) and annealed at 50 °C (5 min). BCP interlayer was also spin-coated at 4000 RPMs (30 s) and annealed at 50 °C (5 min). The copper cathode was deposited with the thermal evaporation method at 2×10^{-6} Torr vacuum level. All devices were encapsulated with UV epoxy from Osilla inc. UV LS processes (P1-P3) were described in the manuscript.

Laser scriber

The laser scriber system was designed by LLC Nordlase (Russia).

Laser type – Nd:YVO_4, 355 nm, impulse – 22 ns at 50kHz. Maximum power – 3W.

The positioning of the samples was realized using motorized XY stage from Standa (1 um resolution in XY movement).

The maximum attenuation of the system – 99%.

During scribing all substrates were fixed with vacuum chuck.

Laser patterning cycle

ITO scribing (P1) was performed using 3 W power at a rate of 5 mm/s (50 kHz, 1 pulse per 3 microns). Electrical isolation between the anode electrodes of the ITO for each pixel in the row was achieved by sequentially conducting 9 passes of the laser beam (50-micron diameter) with an offset of 10 microns.

The P2 process was realized in three passes (5 μm offset) at 1 W power at a speed of 5 mm/s. The width of the scribing line of the P2 process was ~60 μm. After deposition of the metal electrode in a vacuum, the P3 process required the removal of conductive material from the insulating zones between the ITO anode electrodes. Additionally, transverse scribing of the metal electrode was performed to form the final pixel geometry.

The pixel formation, indicated by the transverse metal scribing line in Fig. 2(a) in the manuscript, required the process to be performed at 1 W power, a speed of 2 mm/s, and three passes (10 μm offset). The width of the cut was 40 μm. Electrical isolation between pixels (P3 process) was achieved by ablating the metal contact using the P1 path (side isolation lines according to the top view in Fig. 2(a)). To ensure isolation, scribing was performed at a power of 3 W, speed of 20 mm/s for 1 pass of the laser beam with a cutting width of 40 μm. The P1-P3 patterning processes were the same for PPDs of all configurations.

Characterization

Surface roughness and film thicknesses were measured with KLA-Telencor stylus profilometer.

SEM images were taken in high vacuum at 15 kV accelerating voltage were done with a JEOL JSM7600F system (Tokyo, Japan).

KPFM measurements were performed via NSG10/pt tip calibrated with fresh HOPG (Tip potential = -240 mV)

KPFM mappings were carried out with an Ntegra Prima (NT-MDT SI, Russia) commercial scanning probe using a NSG10/Pt (Tipsnano, Tallinn, Estonia) conductive probe, calibrated with fresh HOPG (Tip potential = -240 mV). For KPFM measurements, the probe scans the surface topography using tapping mode first and then a 1 V AC voltage was applied on the probe near its resonance frequency (□200 kHz) to measure the sample surface potential distribution through a DC voltage feedback loop. The scan rate was set to 0.5 Hz, and a lift scan height of approximately 100 nm was adopted.

Dark JV curves were measured in an ambient atmosphere with Agilent B1500A Semiconductor Device Analyzer (voltage step of 20 mV).

We used LM1-EPG1-11-N2-00001 CREE LED (540 nm) as a light source for estimation of V_{oc}, J_{sc} vs. P_0. The output parameters (Voc, Jsc) were extracted from JV curves measured with Keithley 2400 SMU in 4-wire mode and a settling time of 10−2 s. The LED was connected to a Keysight E36311A source-meter in a hinge-mounted configuration.

Optical power measurements were performed on a ThorLabs S425C. Illuminance measurements were performed on a UPRtek MK350. Completed set up for characterization of PPDs was placed in a black box.

The dynamic response was measured with DIGILENT Analog Discovery Pro 3450 (2 units), which were used as oscilloscope and pulse generator.

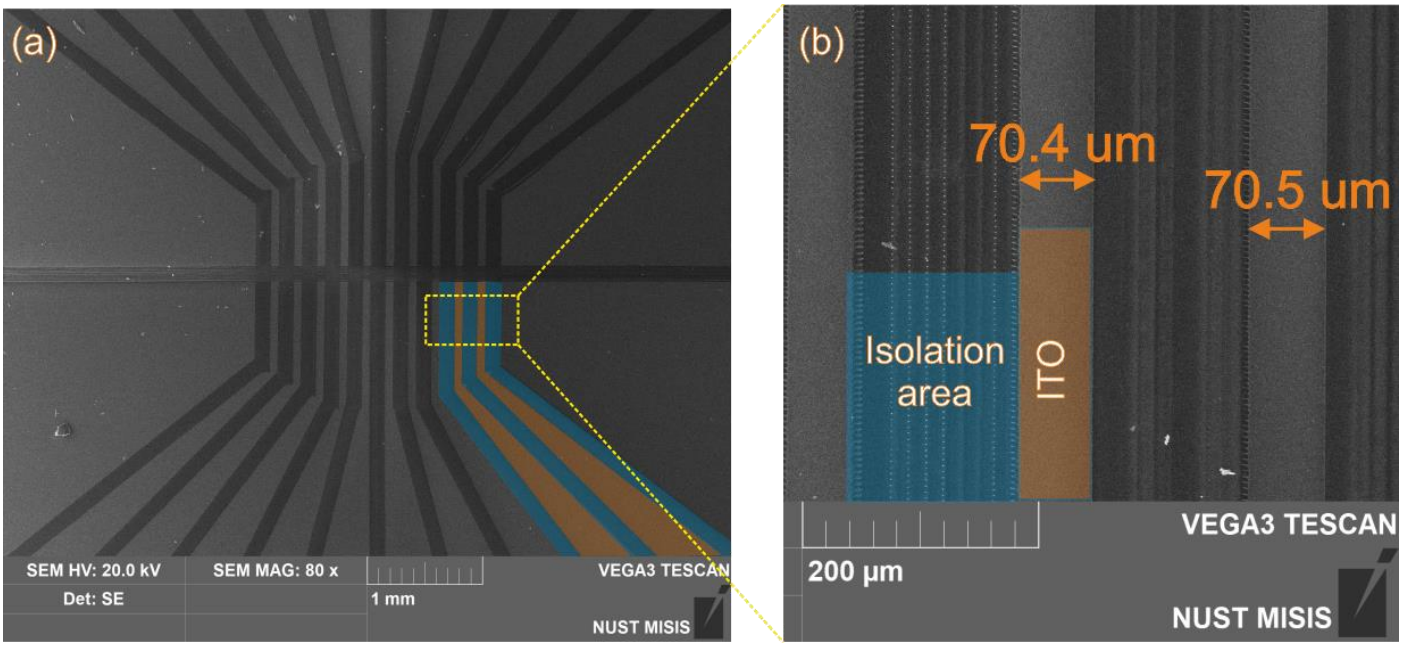

Figure S1 – The SEM image of ITO/Glass scribing after P1 process with 70 um width of anode electrode

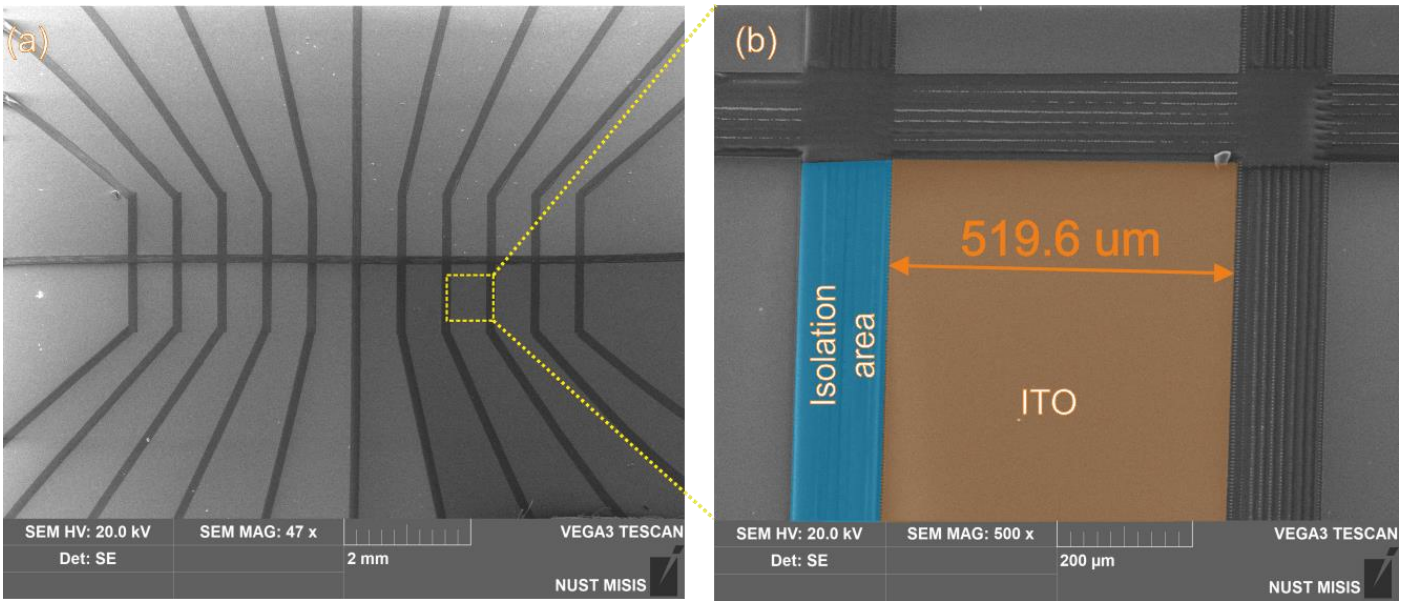

Figure S2 – The SEM image of ITO/Glass scribing after P1 process with 520 um width of anode electrode

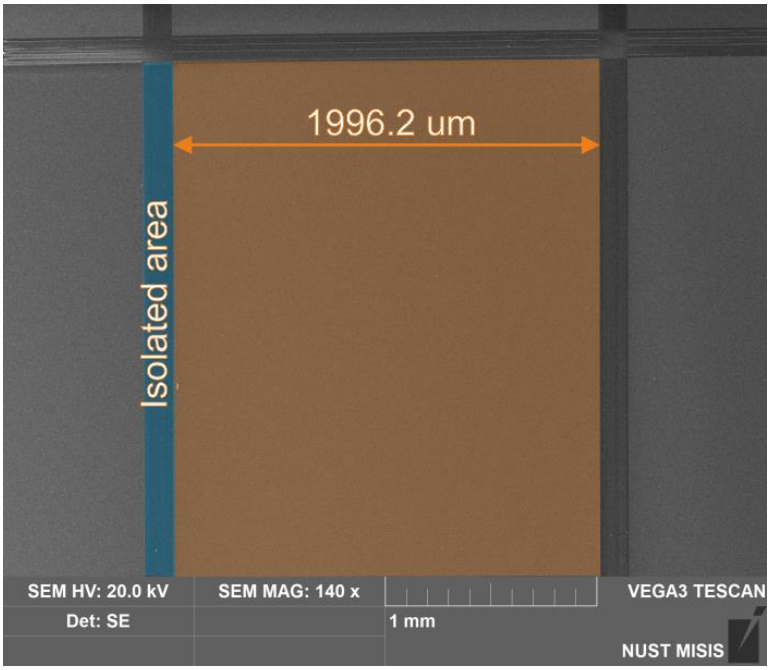

Figure S3 – The SEM image of ITO/Glass scribing after P1 process with 2000 um width of anode electrode

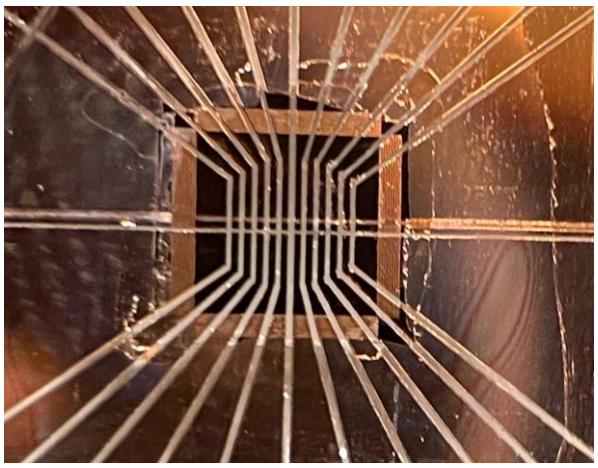

Figure S4 – Photo-image for the string of 10 PPDs with 70x130 um^2 pixels

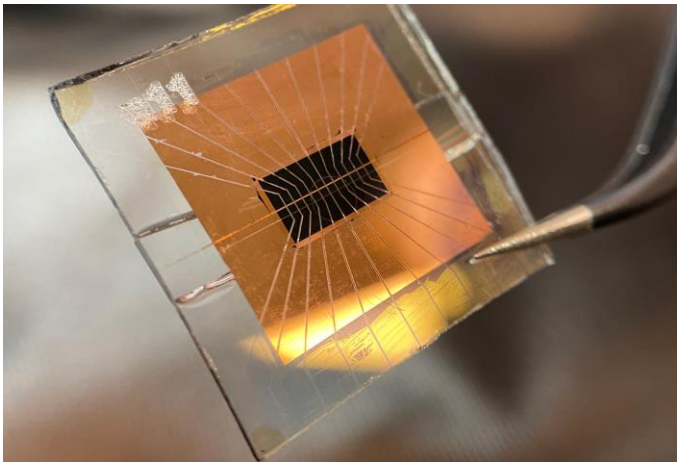

Figure S5 – Photo-image for the string of 10 PPDs with 520x580 um^2 pixels

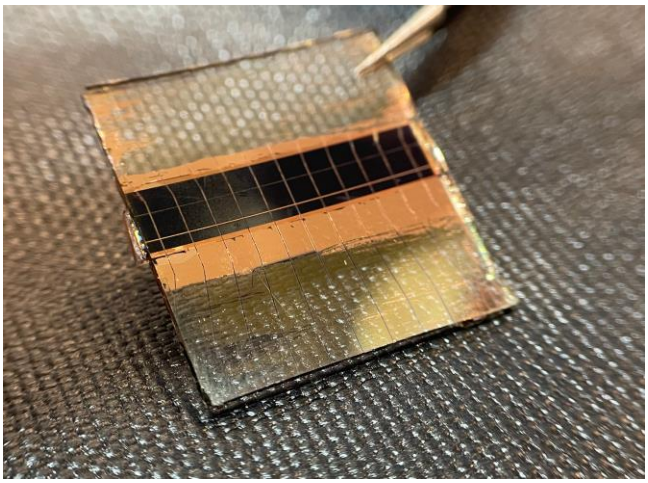

Figure S6 – Photo-image for the string of 10 PPDs with 2000x2000 um^2 pixels

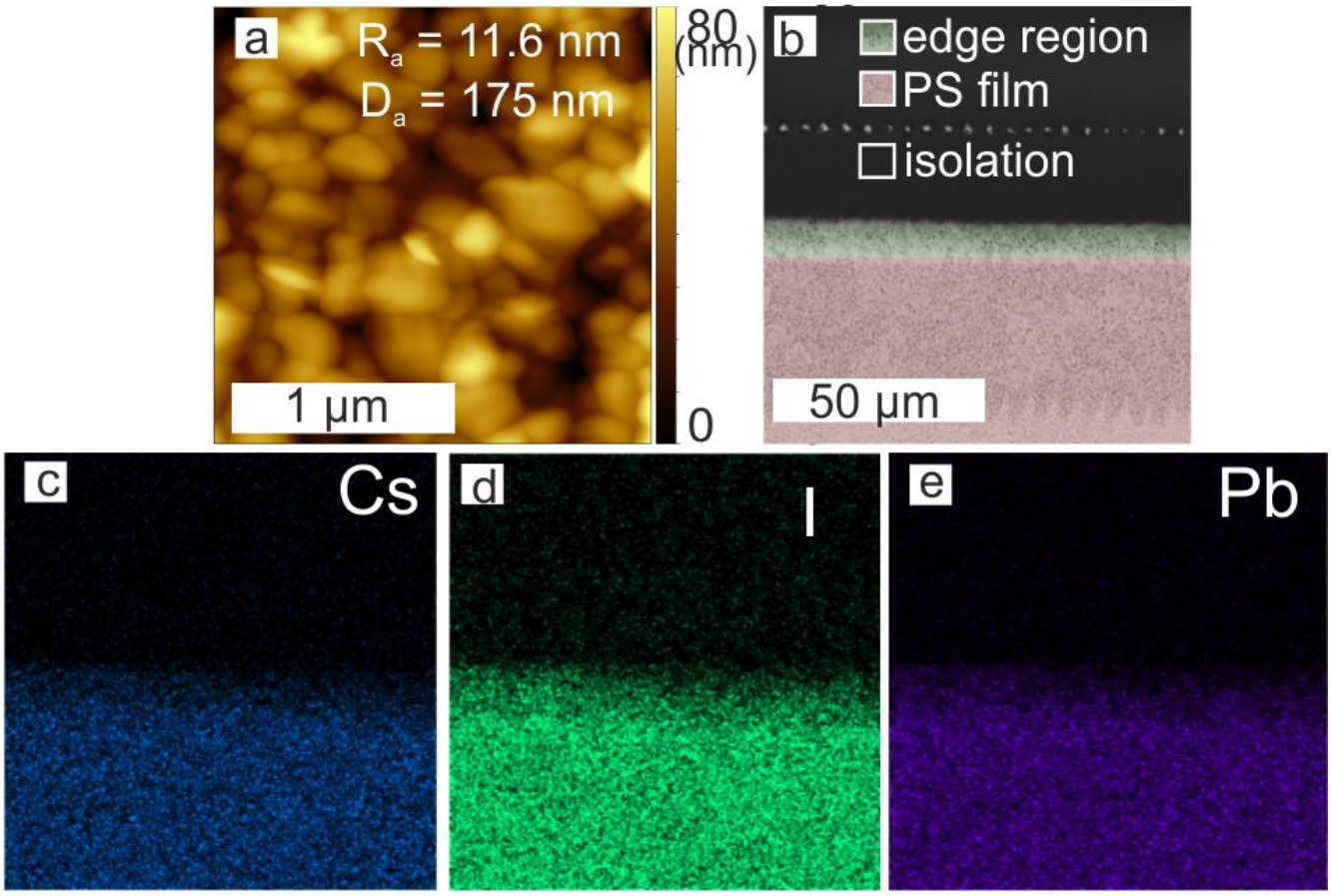

Figure S7 – AFM image of the perovskite absorber (a) SEM image of the edge region in perovskite absorber (b) EDX elemental profiling for Cs (c), I (d) and Pb(e) in the perovskite absorber and edge region

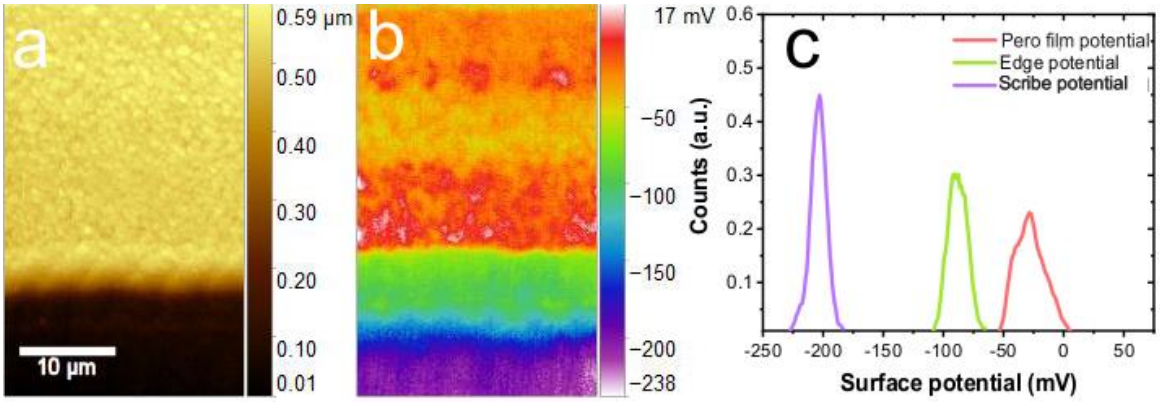

Figure S8 – AFM image with distribution of height (a); heat-map of the surface potential for perovskite film, edge region and scribing area (b); relative changes of the surface potential for perovskite film, edge region and scribing area (c)

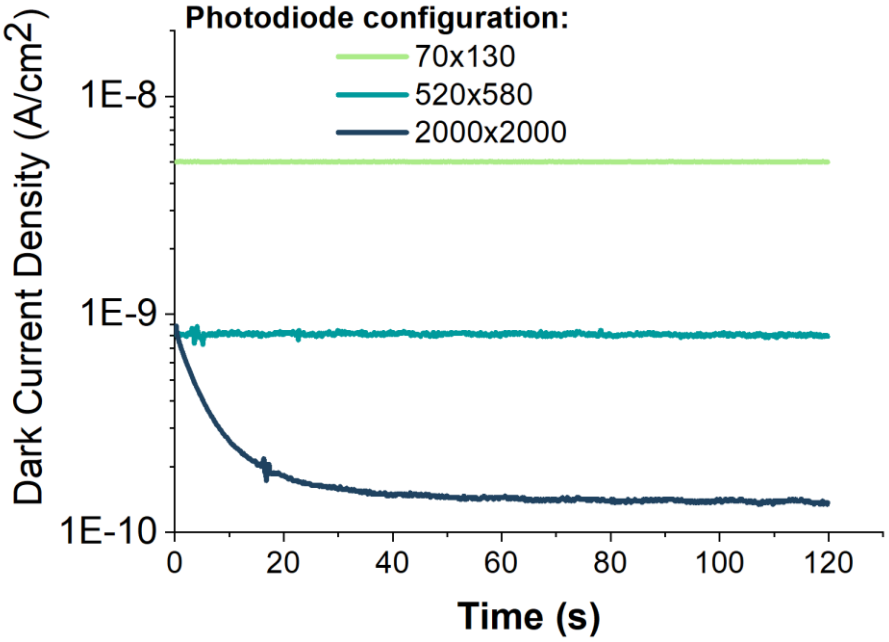

Figure S9 – The stabilization of J_D for various geometries of PPDs with time

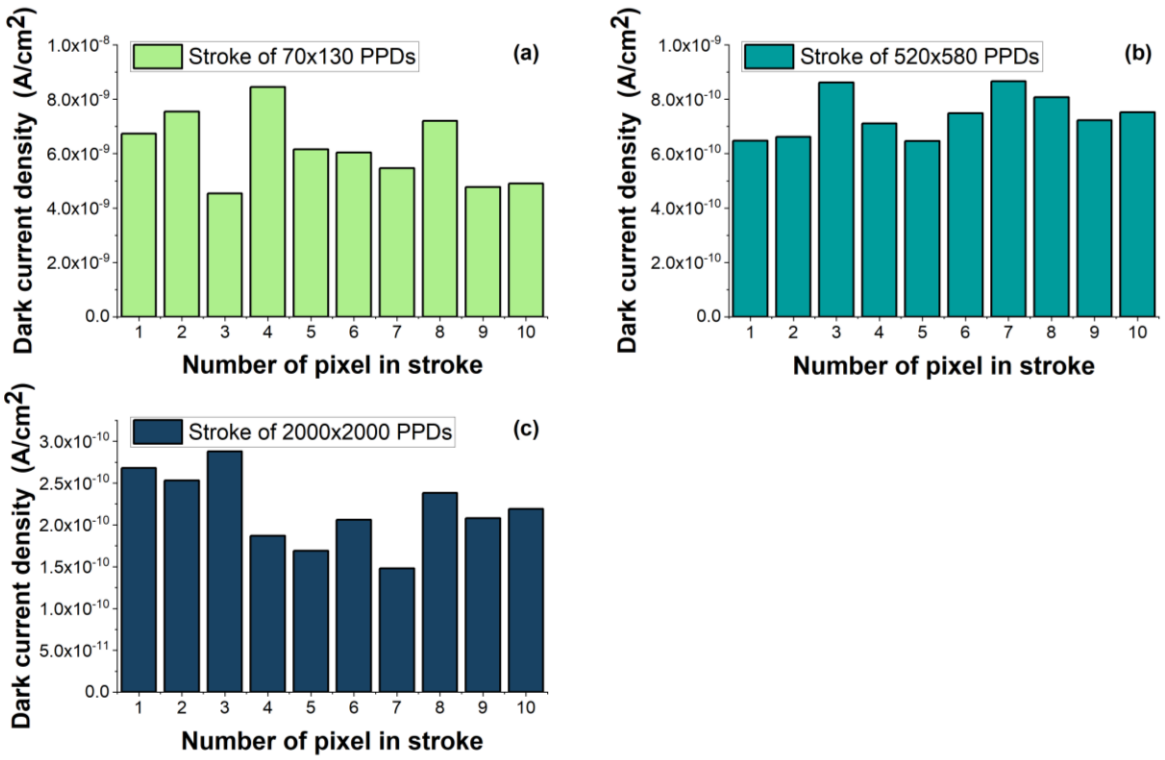

Figure S10 – The distribution of dark current density leakage values for the PPDs in stroke with geometries 70x130 (a); 520x580 (b); and 2000x2000(c)

$$\left|I_{ph}\right| = \eta_{abs}\eta_{qe}\eta_{ce}\frac{q\lambda}{hc}I_L \quad \text{(S1)}^{1}$$

Where I_{ph}- photocurrent;

η_{abs}- absorptance;

η_{abs}- quantu, efficiency for the photogenerated charge carriers;

η_{ce} -charge collection efficiency;

q – elementary charge;

λ- wavelength;

h-Planck's constant;

c – speed of light;

I_L- light intensity.

$$LDR = 20\log\left(\frac{I_{ph}}{I_D}\right) \quad \text{(S2)}$$

Where I_{ph}- photocurrent in linear range

I_D- dark current

$$R = \frac{I_{ph}}{P_0} \quad \text{(S3)}$$

Where I_{ph}- photocurrent (A)

P_0- power of the illumination (W)

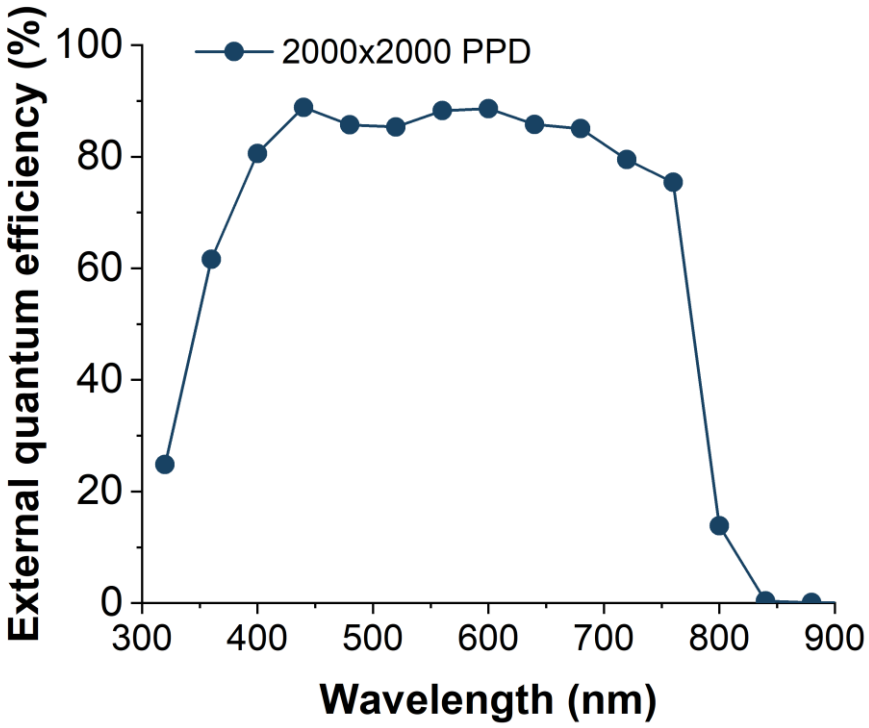

Figure S11 – The external quantum efficiency of 2000x2000 PPD

$$D^* = \frac{I_{ph}\sqrt{A}}{P_0}\left(\frac{1}{(2qJ_d)^{1/2}}\right) \tag{S4}$$

Where A – active area of the device

$$NEP = \frac{(2qJ_d)^{1/2}}{R} \tag{S5}$$

Table S1 – The calculated values of the J_{photo}/J_{dark} for various P_0

P_0 (mW/cm^2)	PPD configuration		
	70x130	520x580	2000x2000
	J_{photo}/J_{dark} ratio		
$2\cdot10^{-3}$	$6.6\cdot10^{1}$	$6.2\cdot10^{2}$	$5.1\cdot10^{3}$
$2\cdot10^{-2}$	$4.5\cdot10^{2}$	$6.6\cdot10^{3}$	$5.5\cdot10^{4}$
$5\cdot10^{-2}$	$1.1\cdot10^{3}$	$1.7\cdot10^{4}$	$1.4\cdot10^{5}$
$1\cdot10^{-1}$	$2.0\cdot10^{3}$	$3.5\cdot10^{4}$	$2.8\cdot10^{5}$
$2\cdot10^{0}$	$3.9\cdot10^{3}$	$6.8\cdot10^{4}$	$5.8\cdot10^{5}$

The active area of a photodiode refers to the light-sensitive region where the charge-transport junction is located. A larger active area means more light can be detected, but it also results in a higher junction capacitance. The photodiode's junction capacitance (**C_J**) varies directly with the active area and inversely with the depletion region width. This junction capacitance, along with any stray capacitances in the circuit, forms an RC time constant with the load resistance, which limits the bandwidth and speed of the photodiode[2]. The frequency response (**f_{3dB}**) expresses the rise time and fall time of a photodiode, indicating the frequency at which the photodiode output decreases by 3dB (**t_r and $t_f \sim 1/ f_{3dB}$**). Charge-carrier transit time (t_{CCT}) and the RC constant determine the value of f_{3dB} (**eq.S6**)[2–4]:

$$f_{-3dB}^{-2} = \left(\frac{3.5}{2\pi t_{CCT}}\right)^{-2} + \left(\frac{1}{2\pi RC}\right)^{-2} \quad \text{(S6)}$$

where R - total series resistance including the device resistance, contact resistances, and load resistances;

C - the sum of the capacitance of the device.

The correlation between f_{3dB} and RC could be approximated as shown in eq.S2:

$$f_{3dB} \sim \frac{1}{2\pi RC} \quad \text{(S7)}$$

As the active area and junction capacitance increase, the RC time constant becomes larger, resulting in a slower rise/fall times and lower bandwidth. Conversely, reducing the active area and junction capacitance can improve the time response and frequency response of the photodiode.

Table S2 – The comparison of the PPDs' output performance with the actual state-of-the-art results

Link	Architecture	Active area (mm^2)	Patterning Method	Dark Current density (A/cm^2) [bias]	D*(Jones) [wavelength]	NEP	Rise time/fall time (microseconds)
[5]	p-i-n ITO/PTAA:polyTPD/$FAMAPb_{0.5}Sn_{0.5}I_3$ /C_{60}/BCP/Ag	1.00	Lithography	5×10^{-11} [-0.5 V]	2.5×10^{12} [940 nm]	2×10^{-14}	0.19 / 0.74
[6]	p-i-n ITO/NiO NP/Cs0.15FA0.85Pb $(I_{0.95}Br_{0.01}7Cl_{0.033})_3$/PCBM/Bphen/Ag	2.5×10^{-3} ($50x50\ um^2$)	Lithography	9.5×10^{-11} [0 V]	1.5×10^{13}	5.6×10^{-16}	48/35
[7]	n-i-p ITO/ZnO NP/$MAPbI_3$ /Spiro/Au	2.5×10^{-3}	Lithography	6×10^{-6} [0 V]	1.35×10^{12}	-	-
[8]	p-i-n ITO/PEDOT:PSS/$MAPbI_3$/PCBM/C60/ BCP/Al	7.25	Lithography/ Masking	5×10^{-10} [0 V] 9×10^{-9} [-1.0 V]	8×10^{13} [680 nm]	4.3×10^{-14}	0.064/0.12
[9]	p-i-n ITO/PTAA/$MAPbI_3$/FBIC/C60/BCP/Cu	44	Lithography/ Masking	9×10^{-10} [0 V] 1×10^{-7} [-0.1 V]	2.3×10^{11}	3.6×10^{-13}	-/ 7.4
[10]	p-i-n	6	Lithography/ Masking	6×10^{-9} [0 V]	1.5×10^{11}	-	900/1800

	ITO/NiO/$MAPbI_3$/PCBM/ZnO NP/BCP/Al			8×10^{-5} [-1.0 V]			
[6]	p-i-n ITO/PTAA/PVP/Perovskite/PCBM/C_{60}/ TiN/Cu	0.1	Lithography/ Masking	3.25×10^{-11} [0 V]	1.21×10^{14} [520 nm]	1.2×10^{-14}	85.2 / 79.3
[11]	p-i-n ITO/PTAA /$CH_3NH_3PbI_3$/IEICO/C_{60}/BCP/Cu	0.6	Lithography/ Masking	2.6×10^{-6} [0 V]	1.45×10^{12} [650 nm]	4×10^{-14}	0.027/0.027
[12]	p-i-n ITO/PTAA /$CH_3NH_3PbI_3$/PCBM/BCP/Ag	4	Lithography/ Masking	9×10^{-11} [0 V]	-	-	14.2 / 14.2
[13]	p-i-n ITO/PEDOT:PSS/$(FASnI_3)_{0.6}(MAPbI_3)_{0.4}$/$C_{60}$/ BCP/Ag	3.8	Lithography/ Masking	9×10^{-11} [0 V]	1.1×10^{12} [900 nm]	1.9×10^{-13}	6.9 / 9.1
[14]	p-i-n ITO/PTAA/PEIE/$CsPbI_2Br$/PCBM/BCP /Ag	0.1	Lithography/ Masking	6×10^{-9} [-0.3 V]	9.7×10^{12} [450 nm]	2.7×10^{-14}	0.020 / 0.276
[15]	n-i-p C/TiO_2/$MAPbI_3$/Cu0/Cu_2O/Cu	2.5	- / Masking	2×10^{-12} [0 V]	1.65×10^{13} [550 nm]		2000.0 / 2000.0
This work	p-i-n ITO/NiO/$CsCH(NH_2)_2PbI_3$/C_{60}/BCP/Cu	9.1×10^{-3} [70 x 130 um^2]	Laser scribing	4.9×10^{-9} [0 V]	6.72×10^{11} [540 nm]	1.42×10^{-14}	0.047 / 0.054
This work	p-i-n ITO/NiO/$CsCH(NH_2)_2PbI_3$/C_{60}/BCP/Cu	0.3 [520 x 580 um^2]	Laser scribing	6.5×10^{-10} [0 V]	4.82×10^{12} [540 nm]	1.14×10^{-14}	0.098 / 0.561
This work	p-i-n ITO/NiO/$CsCH(NH_2)_2PbI_3$/C_{60}/BCP/Cu	4 [2000 x 2000 um^2]	Laser scribing	1.4×10^{-10} [0 V]	1.81×10^{13} [540 nm]	1.10×10^{-14}	2.880 / 3.693

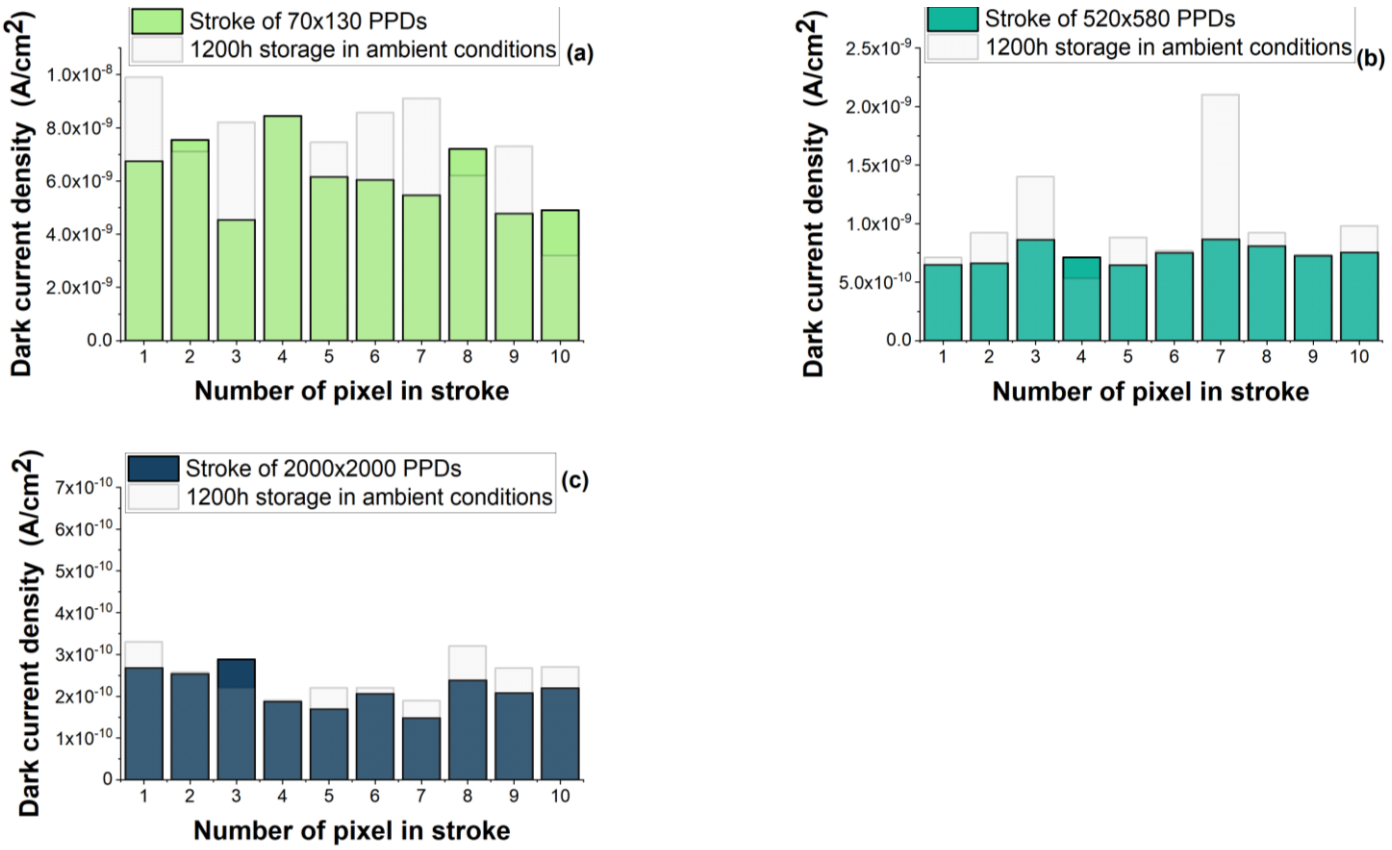

Figure S12 – the evolution of J_{dark} values after storage in the ambient conditions for PPDs with 70x130 geometry (a); 520x580 geometry and 2000x2000 geometry (c)

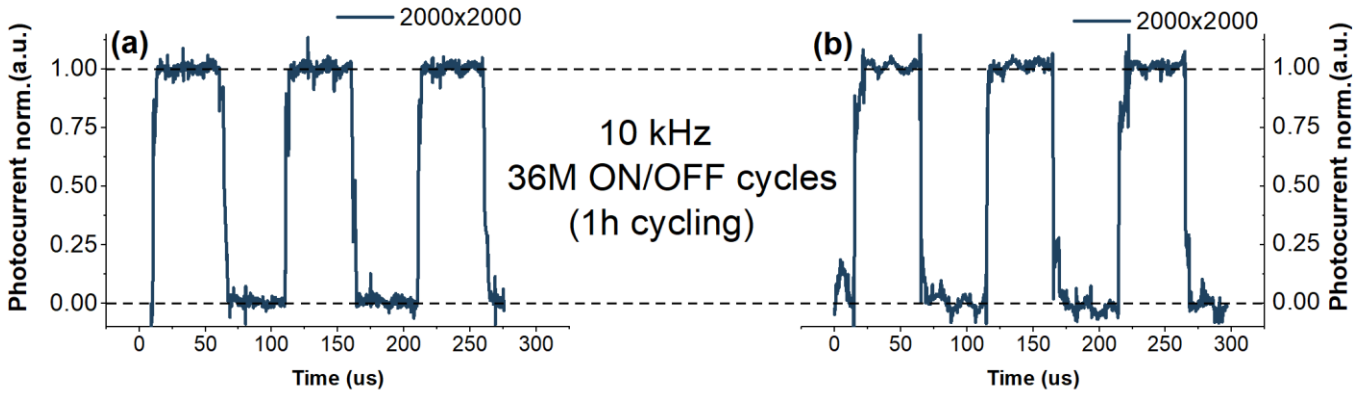

Figure S13 – The evolution of transient photoresponse profiles after 1h of continuous cycling in ON/OFF regime for 2000x2000 PPD

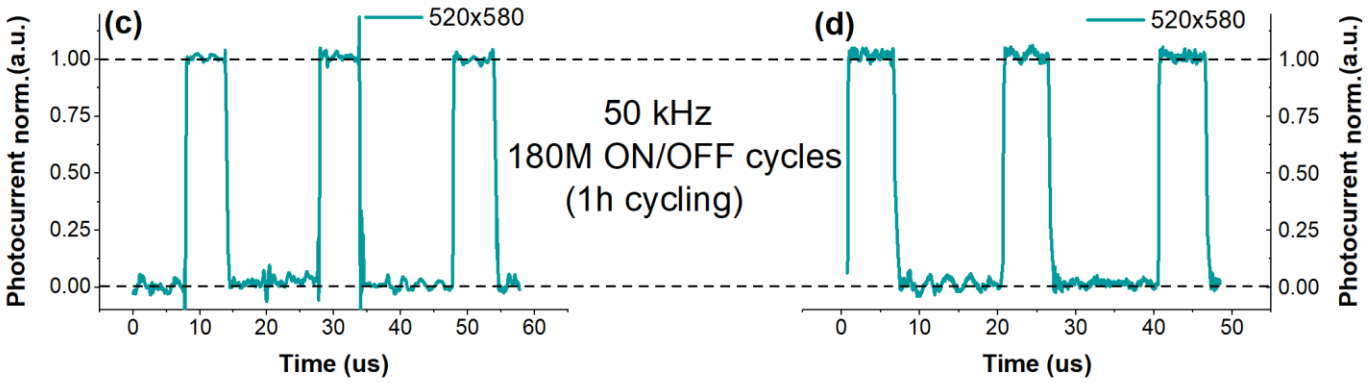

Figure S14 – The evolution of transient photoresponse profiles after 1h of continuous cycling in ON/OFF regime for 520x580 PPD

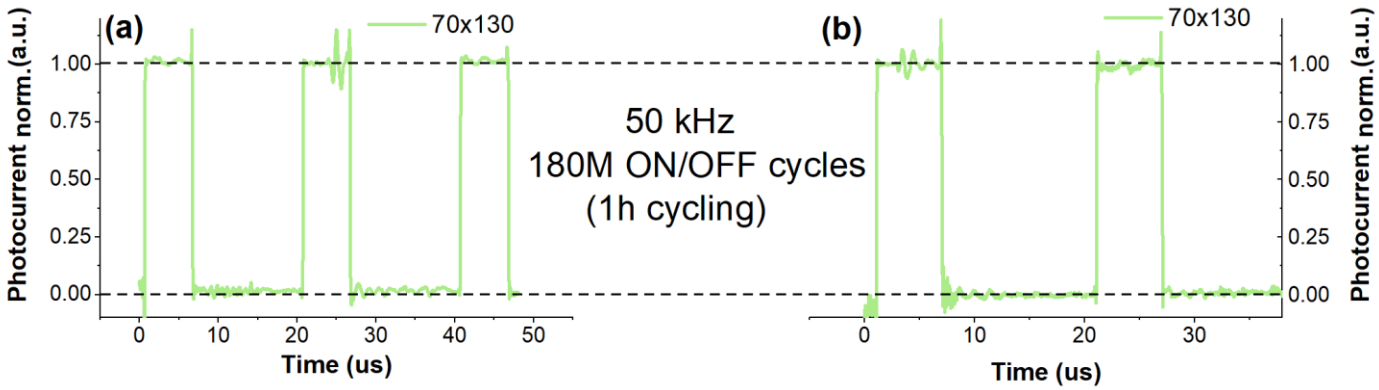

Figure S15 – The evolution of transient photoresponse profiles after 1h of continuous cycling in ON/OFF regime for 70x130 PPD

References:

[1] S. Zeiske, W. Li, P. Meredith, A. Armin, and O.J. Sandberg, “Light intensity dependence of the photocurrent in organic photovoltaic devices,” Cell Rep Phys Sci **3**(10), 101096 (2022).

[2] L. Shen, Y. Fang, D. Wang, Y. Bai, Y. Deng, M. Wang, Y. Lu, and J. Huang, “A Self-Powered, Sub-nanosecond-Response Solution-Processed Hybrid Perovskite Photodetector for Time-Resolved Photoluminescence-Lifetime Detection,” Advanced Materials **28**(48), 10794–10800 (2016).

[3] K. Kato, S. Hata, J. Yoshida, and A. Kozen, “Design of high-speed and high-sensitivity photodiode with an input optical waveguide on semi-insulating InP substrate,” in *LEOS 1992 Summer Topical Meeting Digest on Broadband Analog and Digital Optoelectronics, Optical Multiple Access Networks, Integrated Optoelectronics, and Smart Pixels*, (IEEE, n.d.), pp. 254–257.

[4] A. Armin, M. Hambsch, I.K. Kim, P.L. Burn, P. Meredith, and E.B. Namdas, “Thick junction broadband organic photodiodes,” Laser Photon Rev **8**(6), 924–932 (2014).

[5] R. Ollearo, J. Wang, M.J. Dyson, C.H.L. Weijtens, M. Fattori, B.T. van Gorkom, A.J.J.M. van Breemen, S.C.J. Meskers, R.A.J. Janssen, and G.H. Gelinck, “Ultralow dark current in near-infrared perovskite photodiodes by reducing charge injection and interfacial charge generation,” Nat Commun **12**(1), 7277 (2021).

[6] Y.-Y. Zhang, J.-L. Xu, J.-Y. Zhang, Y. Yuan, X. Gao, and S.-D. Wang, “Small-Area Perovskite Photodiodes With High Detectivity and Stability,” IEEE Electron Device Letters **42**(8), 1200–1203 (2021).

[7] W. Lee, J. Lee, H. Yun, J. Kim, J. Park, C. Choi, D.C. Kim, H. Seo, H. Lee, J.W. Yu, W.B. Lee, and D. Kim, “High-Resolution Spin-on-Patterning of Perovskite Thin Films for a Multiplexed Image Sensor Array,” Advanced Materials **29**(40), (2017).

[8] Y. Fang, and J. Huang, “Resolving Weak Light of Sub-picowatt per Square Centimeter by Hybrid Perovskite Photodetectors Enabled by Noise Reduction,” Advanced Materials **27**(17), 2804–2810 (2015).

[9] C. Li, H. Wang, F. Wang, T. Li, M. Xu, H. Wang, Z. Wang, X. Zhan, W. Hu, and L. Shen, “Ultrafast and broadband photodetectors based on a perovskite/organic bulk heterojunction for large-dynamic-range imaging,” Light Sci Appl **9**(1), 31 (2020).

[10] A.M. Afzal, I.-G. Bae, Y. Aggarwal, J. Park, H.-R. Jeong, E.H. Choi, and B. Park, “Highly efficient self-powered perovskite photodiode with an electron-blocking hole-transport NiOx layer,” Sci Rep **11**(1), 169 (2021).

[11] T. Sun, T. Chen, J. Chen, Q. Lou, Z. Liang, G. Li, X. Lin, G. Yang, and H. Zhou, “High-performance p–i–n perovskite photodetectors and image sensors with long-term operational stability enabled by a corrosion-resistant titanium nitride back electrode,” Nanoscale **15**(17), 7803–7811 (2023).

[12] C. Li, J. Lu, Y. Zhao, L. Sun, G. Wang, Y. Ma, S. Zhang, J. Zhou, L. Shen, and W. Huang, “Highly Sensitive, Fast Response Perovskite Photodetectors Demonstrated in Weak Light Detection Circuit and Visible Light Communication System,” Small **15**(44), (2019).

[13] T. Zou, B. Xiang, Y. Xu, Y. Wang, C. Liu, J. Chen, K. Wang, Q. Dai, S. Zhang, Y.-Y. Noh, and H. Zhou, “Pixellated Perovskite Photodiode on IGZO Thin Film Transistor Backplane for Low Dose Indirect X-Ray Detection,” IEEE Journal of the Electron Devices Society **9**, 96–101 (2021).

[14] W. Wang, D. Zhao, F. Zhang, L. Li, M. Du, C. Wang, Y. Yu, Q. Huang, M. Zhang, L. Li, J. Miao, Z. Lou, G. Shen, Y. Fang, and Y. Yan, “Highly Sensitive Low-Bandgap Perovskite Photodetectors with Response from Ultraviolet to the Near-Infrared Region,” Adv Funct Mater **27**(42), (2017).

[15] C. Bao, J. Yang, S. Bai, W. Xu, Z. Yan, Q. Xu, J. Liu, W. Zhang, and F. Gao, “High Performance and Stable All-Inorganic Metal Halide Perovskite-Based Photodetectors for Optical Communication Applications,” Advanced Materials **30**(38), (2018).

[16] H. Sun, W. Tian, F. Cao, J. Xiong, and L. Li, “Ultrahigh-Performance Self-Powered Flexible Double-Twisted Fibrous Broadband Perovskite Photodetector,” Advanced Materials **30**(21), (2018).